Engineering Science & Technology
https://ojs.wiserpub.com/index.php/EST/

UNIVERSAL WISER PUBLISHER

Research Article

Design of Asymmetric Janus Aerogel Toward High-Performance Solar Evaporation

Liumin Luo[1], Airong Wang[2*], Luhan Zheng[3], Xiaxuan Jia[3], Ge Shi[3], Yizhen Li[3], Jin Peng[3], Mengya Shang[3†]

[1]College of Information Engineering, Luoyang Polytechnic, Luoyang, Henan Province, 471003, China
[2]School of Electro-Mechanical Engineering, Zhongyuan Institute of Science and Technology, Xuchang, Henan Province, 461000, China
[3]School of Material Science and Engineering, Henan University of Technology, Zhengzhou, Henan Province, 450001, China
E-mail: wair@hist.edu.cn; mengyashang@haut.edu.cn

Received: 19 May 2026; **Revised:** 22 June 2026; **Accepted:** 10 July 2026

Abstract: Interfacial solar evaporation technology enables high-efficiency evaporation with low energy consumption through solar-driven localized heating and has broad application prospects in seawater desalination and industrial wastewater treatment. As novel functional materials with asymmetric physicochemical characteristics, Janus aerogels provide a new approach for overcoming the performance limitations of traditional evaporators. In this work, a Janus aerogel was fabricated using Polyvinyl Alcohol/Cellulose Nanofiber (PVA/CNF) as the substrate and Carbon Nanotubes (CNT) as the photothermal layer. Owing to its asymmetric structure, which integrates hydrophilic water transport and hydrophobic photothermal characteristics, the resulting aerogel achieves efficient photothermal conversion and directional water delivery. Its maximum surface temperature reaches 64.4 °C with a light absorption efficiency of 99%, consistent with the finite element simulation results. Under 1 sun, the evaporation rate is 1.32 $kg \cdot m^{-2} \cdot h^{-1}$ and the corresponding evaporation efficiency is 88.37%, and the aerogel maintains stable evaporation performance over 7 cycles, with only minor salt precipitation on the surface after 2 h of irradiation. This developed material shows promising potential in seawater desalination and wastewater purification, offering a novel strategy for the rational design of multifunctional aerogel evaporators.

***Keywords*:** Janus aerogel, carbon nanotube, photothermal conversion, solar interfacial evaporation, finite element simulation

1. Introduction

As the global water shortage crisis continues to intensify, the development of efficient and sustainable water treatment technologies has become a central focus for research and industry. Solar energy, as an inexhaustible and widely distributed clean energy source, is regarded as a key pathway to addressing the dual crises of water and energy [1]. Interfacial solar evaporation technology, leveraging its unique advantage of converting solar energy into localized heat to drive efficient water evaporation at the liquid-vapor interface, demonstrates significant application potential in seawater desalination and industrial wastewater treatment [2], [3]. However, conventional evaporator materials still face severe heat loss to the bulk water, salt accumulation and clogging at the evaporation interface, and poor long-term

DOI: https://doi.org/10.37256/est.81202710178

operational stability in practical applications, severely restricting their continuous and efficient operation [4]. Therefore, designing novel evaporator materials with functional zoning and synergistic regulation capabilities has become key to improving interfacial evaporation performance.

Photothermal materials are the core components for achieving efficient solar energy conversion. Based on their working mechanisms, they can be classified into carbon-based materials [5], semiconductor materials [6], metallic materials [7], and organic polymer materials [8], [9]. Among them, carbon-based materials such as graphene [10] and Carbon Nanotubes (CNTs) [11] have attracted extensive attention due to their broad-spectrum light absorption and excellent photothermal conversion efficiency, leading to a series of breakthrough advances in solar-driven water evaporation. Wang et al. [12] incorporated carbon nanodots into a porous matrix and achieved a water evaporation rate of 2.31 $kg \cdot m^{-2} \cdot h^{-1}$ under 1 sun. Wang et al. [13] fabricated a suspended photothermal fabric using polyaniline/carbon nanotube composites; this structure reduced heat loss and achieved a solar water evaporation rate as high as 2.81 $kg \cdot m^{-2} \cdot h^{-1}$ with a photothermal conversion efficiency of 91.74%. Liu et al. [14] prepared a bilayer composite aerogel using carboxymethyl cellulose as the skeleton and carbon nanotubes as the photothermal material, achieving an evaporation rate of 1.942 $kg \cdot m^{-2} \cdot h^{-1}$ under 1 sun. Ji et al. [15] developed a thermo-responsive composite hydrogel based on carboxylated carbon nanotubes, which exhibited high swelling capacity, salt resistance, and long-term cycling stability. Under 1 sun, this hydrogel achieved evaporation rates of 2.35 $kg \cdot m^{-2} \cdot h^{-1}$ in pure water and 1.71 $kg \cdot m^{-2} \cdot h^{-1}$ in brine.

However, single-material systems often struggle to simultaneously meet the integrated demands of high-efficiency photothermal conversion, stable water transport, and salt accumulation resistance. To overcome the performance bottlenecks of single materials, Janus materials have attracted widespread attention due to their asymmetric structure with different chemical compositions or physical properties on two sides [16]. Their unique functional partitioning into "hydrophobic photothermal" and "hydrophilic water-transport" layers provides a new paradigm for designing interfacial evaporation materials: the hydrophobic photothermal layer localizes heat at the evaporation interface, reducing heat loss to the bulk water, while the hydrophilic water-transport layer continuously supplies water via capillary action and simultaneously inhibits salt accumulation on the surface. This asymmetric design provides a structural basis for enhancing evaporation efficiency and prolonging material lifetime. Aerogels, as three-dimensional porous materials with high porosity, low density, and low thermal conductivity, are considered ideal substrates for constructing Janus-structured evaporators [17]. Wang et al. [18] constructed a three-dimensional Janus-type MXene/Cellulose Nanofiber (CNF)/loofah aerogel that combines ultrahigh mechanical strength, excellent salt resistance, and high desalination efficiency. Under 1 sun, this material achieved an evaporation rate of 1.40 $kg \cdot m^{-2} \cdot h^{-1}$, demonstrating its applicability in solar-driven interfacial evaporation and seawater purification.

In this study, a Janus aerogel was designed based on a CNF/Polyvinyl Alcohol (PVA) aerogel substrate and a CNT photothermal layer. The hydrophilic three-dimensional CNF/PVA network serves as the water-transport and support layer, ensuring continuous water supply, while the hydrophobic CNT photothermal layer functions as the light absorption and heat-conversion layer, enabling efficient solar harvesting and heat localization. The microstructure, hydrophilicity/hydrophobicity, light absorption performance, photothermal conversion characteristics, and indoor evaporation behavior of the Janus aerogel were systematically investigated. Furthermore, its salt resistance and cycling stability were comprehensively evaluated. This study not only provides a new strategy for the design of multifunctional aerogels but also offers experimental support for performance optimization and structural innovation of interfacial solar evaporation materials.

2. Experimental

2.1 *Materials*

Polyvinyl Alcohol (PVA1799), Sodium Dodecylbenzenesulfonate (SDBS), and sodium chloride (NaCl) were purchased from Shanghai Macklin Biochemical Technology Co., Ltd. Cellulose Nanofibers (CNF) were obtained from NanoFC Co., Ltd. Multi-Walled Carbon Nanotubes (MWCNTs) were purchased from Suzhou Tanfeng Technology Co., Ltd. All reagents were used as received without further purification.

2.2 *Preparation of CNT/PVA/CNF aerogel*

10 g of PVA was added to 90 g of deionized water and stirred at 95 °C for 3 h until complete dissolution. 45 g of CNF solution (4.5 wt%) was added to the above 10% PVA solution at a CNF-to-PVA mass ratio of 1 : 5, followed by stirring for 1 h to obtain a homogeneous mixture. The mixture was then poured into a Petri dish and frozen in a refrigerator for 24 h. After freezing, the sample was transferred to a freeze dryer and freeze-dried at -70 °C for 72 h to obtain the CNF/PVA aerogel.

0.1 g of CNT was dispersed in 10 g of an aqueous solution SDBS, followed by ultrasonication at 300 W for 1 h to achieve uniform dispersion, and then centrifuged three times. The centrifuged product was dried in a vacuum oven at 50 °C for 4 h, and then dispersed in deionized water at a CNT-to-water mass ratio of 1 : 100 to prepare the CNT dispersion. The CNT dispersion was applied onto the surface of the CNF/PVA aerogel using a spraying device (OLF800W) by multiple thin-layer spray coatings, with spraying amounts of 0.039 g, 0.045 g, and 0.060 g, the corresponding mass fractions of CNT relative to the PVA/CNF aerogel are 6 wt%, 7 wt%, and 9 wt%, and the resultant samples are designated as 6% CPC, 7% CPC, and 9% CPC, respectively. A 5 min interval was allowed between each spraying. After natural drying, the samples were further dried in a vacuum oven at 50 °C for 4 h. The experimental procedure is illustrated in Figure 1.

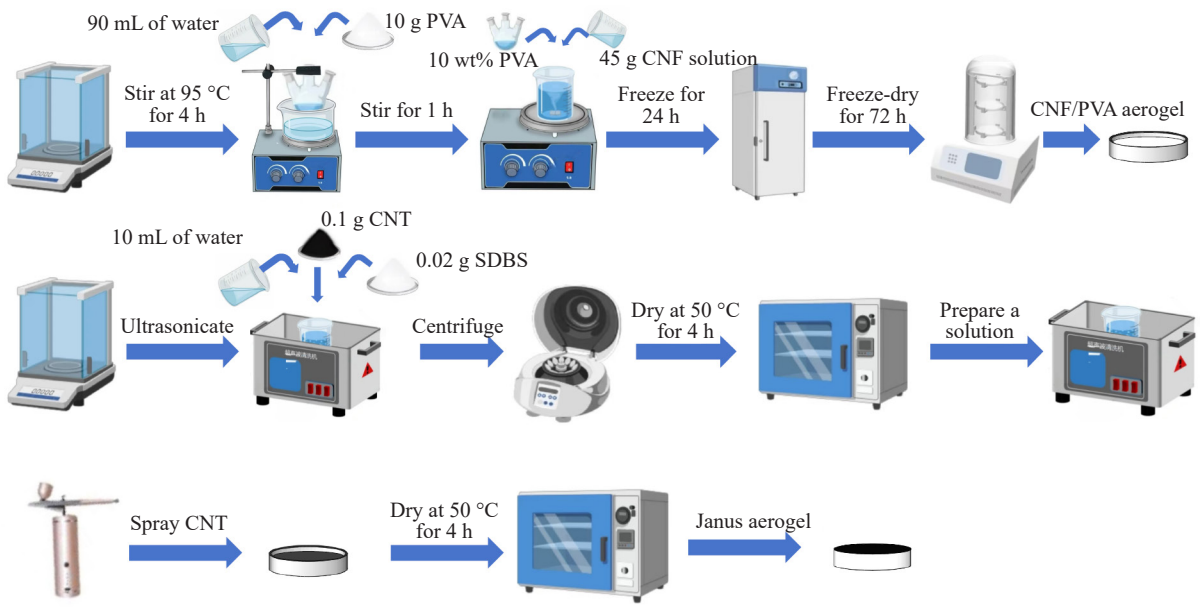

Figure 1. Schematic diagram of the experimental preparation process

2.3 *Material characterization*

Optical photographs of the samples were recorded using a digital camera. The morphology of the aerogels was characterized using a high-resolution field-emission Scanning Electron Microscope (SEM) (FEINSPECT F50) to observe their microstructure. Fourier-Transform Infrared spectra (FTIR) were recorded from 4,000 cm^{-1} to 400 cm^{-1} on an IRPrestige-21 spectrometer to identify the functional groups of the samples. X-Ray Diffraction (XRD) patterns were obtained using an X-ray diffractometer (MINIFLEX600) at a scanning rate of 5° per minute over a diffraction angle range of 0-90° with the CNTs layer upward. The concentrations of Na^+, K^+, Ca^{2+} and Mg^{2+} in the original simulated seawater and the collected condensate were determined by inductively coupled plasma optical emission spectrometry (Agilent-7900). Differential scanning calorimetry (DSC200F3) was performed under a nitrogen atmosphere to investigate the variation of water evaporation enthalpy in the Janus-type aerogel, with a heating rate of 10 °C·min^{-1} from 25 °C to 200 °C. The thermal stability of the samples was evaluated using a Thermogravimetric Analyzer (TGA)

(model ZRT-2, Jingyi Gaoke) under an air atmosphere, with a temperature range from 25 °C to 600 °C and a heating rate of 10 °C/min. Specimens for the FTIR, Differential Scanning Calorimetry (DSC), Thermogravimetric (TG) analysis were taken from intact Janus aerogel films that contain upper layer and substrate layer. For FTIR spectroscopy, a small piece of the intact Janus aerogel film, encompassing both the upper CNT photothermal layer and the lower PVA/CNF base layer (as depicted in the side view of Figure 2b in Section 3.1), was excised. The sample was then ground into a powder, mixed with KBr, and pressed into a pellet for analysis. For XRD analysis, a small piece of the intact Janus aerogel film (approximately 10 × 10 mm, comprising both layers) was cut, flattened, and directly placed onto the sample stage for testing without grinding (CNTs layer upward). For DSC measurement, a small piece of the intact Janus aerogel film (approximately 5-10 mg, containing both layers) was directly sealed within an aluminum crucible for testing. A contact angle goniometer (JC2000D28) was used to measure the surface wettability of the samples with a 4 μL droplet. Photothermal conversion performance was tested using a 3A solar simulator xenon light source (PE300L-3A), with the light intensity recorded by an optical power meter (CEL-FZ-A). The temperature was monitored and recorded using an infrared thermal imager (Fotric 326Pro). The solar light absorption performance of the aerogels (CNTs layer) was measured using a Ultraviolet-Visible-Near Infrared (UV-Vis-NIR) spectrometer (UV-2006i) in the wavelength range of 200 nm to 1,400 nm. The transmittance (T) and absorptance (A) were calculated as follows:

$$A = -\lg T \tag{1}$$

$$\alpha = (1-10^{-A}) \times 100\% \tag{2}$$

where α is the absorption efficiency (Note that the reflection of the aerogel is ignored in this calculation).

2.4 *Evaporation performance test*

Simulated seawater with an initial salinity of 3.5% was prepared. The aerogel evaporator was placed on the surface of a glass container filled with 100 mL of the simulated seawater, and surrounded by a Polystyrene (PS) foam insulation cover to construct a closed evaporation system. The entire experiment was conducted under constant temperature and humidity conditions (25 ± 0.5 °C, Relative Humidity (RH) 30 ± 2%). A precision electronic balance was used to monitor the mass change of the evaporation system in real time. The evaporation rate per unit area (v) and evaporation efficiency (η) were calculated based on the time-mass curve using the following formulas:

$$v = \frac{\Delta m}{A \Delta t} \tag{3}$$

$$\eta = \frac{m h_{LV}}{C_{opt} q_i} \tag{4}$$

where Δm is the mass loss of the evaporator (kg), A is the solar radiation receiving area of the evaporator (m^2), h_{LV} is the total enthalpy of liquid-vapor phase change of water (2,410 $kJ \cdot kg^{-1}$), C_{opt} is the standard solar irradiance (1 $kW \cdot m^{-2}$), and q_i is the actual incident light intensity ($kW \cdot m^{-2}$). Using simulated seawater as the treatment medium, the aerogel evaporator was continuously irradiated under 1 sun for 2 h, during which salt precipitation and crystallization behavior were monitored in real time. Simultaneously, the mass change of the system was recorded to calculate the long-term evaporation rate. The salt resistance, cyclic stability, and reusability of the material were comprehensively evaluated to verify its long-term application potential in practical seawater desalination scenarios.

2.5 *Finite element simulation*

A multiphysics coupling model based on the finite element method was employed to numerically analyze the photothermal performance and temperature distribution of the aerogel. The computational domain comprises three

parts: a PS foam insulating layer, the composite aerogel, and the surrounding ambient air. This model replicates the experimental configuration, in which the aerogel is supported by a PS foam block to minimize conductive heat loss to the underlying bulk water. Accordingly, the simulated temperature distribution can accurately characterize the practical photothermal performance and heat localization behavior of the Janus aerogel. The model incorporates strong coupling between two physical interfaces: laminar flow and heat transfer in solids and fluids. To replicate photothermal conversion under 1 sun, a heat flux of 1 $kW \cdot m^{-2}$ was applied to the top surface of the aerogel. Heat transfer occurs through thermal conduction within the solid regions (the aerogel and PS foam) and convective heat transfer at the air-solid boundaries. The laminar flow interface was used to simulate natural convection of the ambient air induced by temperature gradients, thereby accurately describing heat dissipation to the surroundings. The temperature field and airflow velocity distribution were derived by solving the Navier-Stokes equations and the energy equation simultaneously.

For laminar flow:

$$p\frac{\partial u}{\partial t} + \rho(u \cdot \nabla)u = \nabla \cdot [-pI + \mu(\nabla u + (\nabla u)^T)] + F + \rho g \tag{5}$$

$$\rho \nabla \cdot u = 0 \tag{6}$$

In these expressions, u denotes the fluid velocity, ρ is the density, p represents the fluid stress tensor, I is the identity tensor matrix, F stands for the applied body force, μ indicates the viscosity, and g is the gravitational acceleration constant.

For heat transfer:

$$\rho C_p \frac{\partial T}{\partial t} + \rho C_p u \cdot \nabla T + \nabla \cdot q = Q \tag{7}$$

$$q = -k\nabla T \tag{8}$$

In these equations, T denotes temperature, C_p is the specific heat capacity at constant pressure, q stands for the heat flux, k represents the thermal conductivity coefficient, and Q is the heat source term.

For heat radiation:

$$Q_{rad} = \varepsilon A(G - J) \tag{9}$$

$$J = \sigma(T^4 - T_{amb}^4) \tag{10}$$

In this expression, Q_{rad} denotes the radiative heat, ε the surface emissivity, A the radiative surface area, G the incident solar irradiation, J the surface radiosity, σ the Stefan-Boltzmann constant, and T_{amb} the ambient temperature. The simulation parameters are presented in Table 1.

The boundary conditions are defined as follows: the top surface is subjected to a heat flux of 1 $kW \cdot m^{-2}$; the bottom surface is thermally insulated by a PS foam layer; the side surfaces are exposed to the ambient environment; the ambient temperature is set to 298.15 K (25 °C); and natural convection is considered with a heat transfer coefficient of h = 5 $W \cdot m^{-2} \cdot K^{-1}$. The porosity was estimated based on the SEM morphology and typical values reported for similar PVA/CNF aerogels in the literature [19]. Direct measurement of the porosity will be performed in future work.

Table 1. Key parameters employed in the finite element simulation

Parameter	Value
Thermal conductivity of CPC aerogel	1.56 $W \cdot m^{-1} \cdot K^{-1}$
Specific heat capacity of CPC aerogel	4,200 $J \cdot kg^{-1} \cdot K^{-1}$
Density of CPC aerogel	130 $kg \cdot m^{-3}$
Porosity of CPC aerogel	96.8%
Thermal conductivity of PS foam	0.035 $W \cdot m^{-1} \cdot K^{-1}$
Air density	1.225 $kg \cdot m^{-3}$
Surface emissivity	0.95
Initial temperature	298.15 K

2.6 *Heat loss calculation*

The conductive heat flux (Q_{cond}) from the aerogel to the bulk water is given by the following equation:

$$Q_{cond} = C \cdot m \cdot \Delta T \tag{11}$$

In the above expressions, C denotes the specific heat capacity of water (4.18 $J \cdot g^{-1} \cdot K^{-1}$), m is the mass of the bulk water (0.05 kg), and ΔT indicates the temperature increase of the bulk water after stable steam generation.

The radiative heat transfer is determined by the Stefan-Boltzmann equation:

$$Q_{rad} = \varepsilon \cdot S \cdot \sigma \cdot (T^4 - T_{amb}^4) \tag{12}$$

In this equation, Q_{rad} denotes the thermal radiation flux, ε is the emissivity, S represents the evaporation area (7.07 $\times$ 10^{-4} m^2), σ stands for the Stefan-Boltzmann constant (5.67 $\times$ 10^{-8} $W \cdot m^{-2} \cdot K^{-4}$), T refers to the steady-state temperature of the CPC sample under 1 standard sun, and T_{amb} is the ambient temperature (298.15 K).

The convective heat transfer, H_{conv}, is determined using Newton's law of cooling:

$$H_{conv} = \alpha \cdot S \cdot (T - T_{amb}) \tag{13}$$

Here, α denotes the convective heat transfer coefficient, taken as 5 $W \cdot m^{-2} \cdot K^{-1}$.

Heat Loss Contribution Rate:

$$\eta = \frac{Q}{P} \times 100\% \tag{14}$$

In this expression, Q represents the three components of heat loss—namely, the conductive heat flux (Q_{cond}), the thermal radiation flux (Q_{rad}), and the convective heat flux (H_{conv})—and their respective contribution ratios are denoted as η_1, η_2, and η_3. P is the total incident light power on the evaporation surface (0.803 W).

3. Results and discussion

3.1 *Morphology and microstructure*

As illustrated in the evaporation mechanism diagram of the aerogel shown in Figure 2a, the upper CNT photothermal layer of the Janus aerogel efficiently absorbs solar light and converts it into thermal energy, creating a localized high-temperature region at the liquid-vapor interface. Meanwhile, the lower PVA/CNF aerogel, through capillary action facilitated by abundant hydroxyl groups, enables continuous directional transport of seawater toward the evaporation interface and rapid vaporization. Finally, the asymmetric wettability of the Janus structure allows the hydrophobic CNT layer to inhibit salt deposition and the hydrophilic PVA/CNF layer to promote salt backflow, effectively alleviating salt accumulation. Consequently, the low thermal conductivity of the three-dimensional porous PVA/CNF skeleton enables heat localization and reduces heat loss to the bulk water. These three factors synergistically ensure efficient and stable solar water evaporation performance of the system.

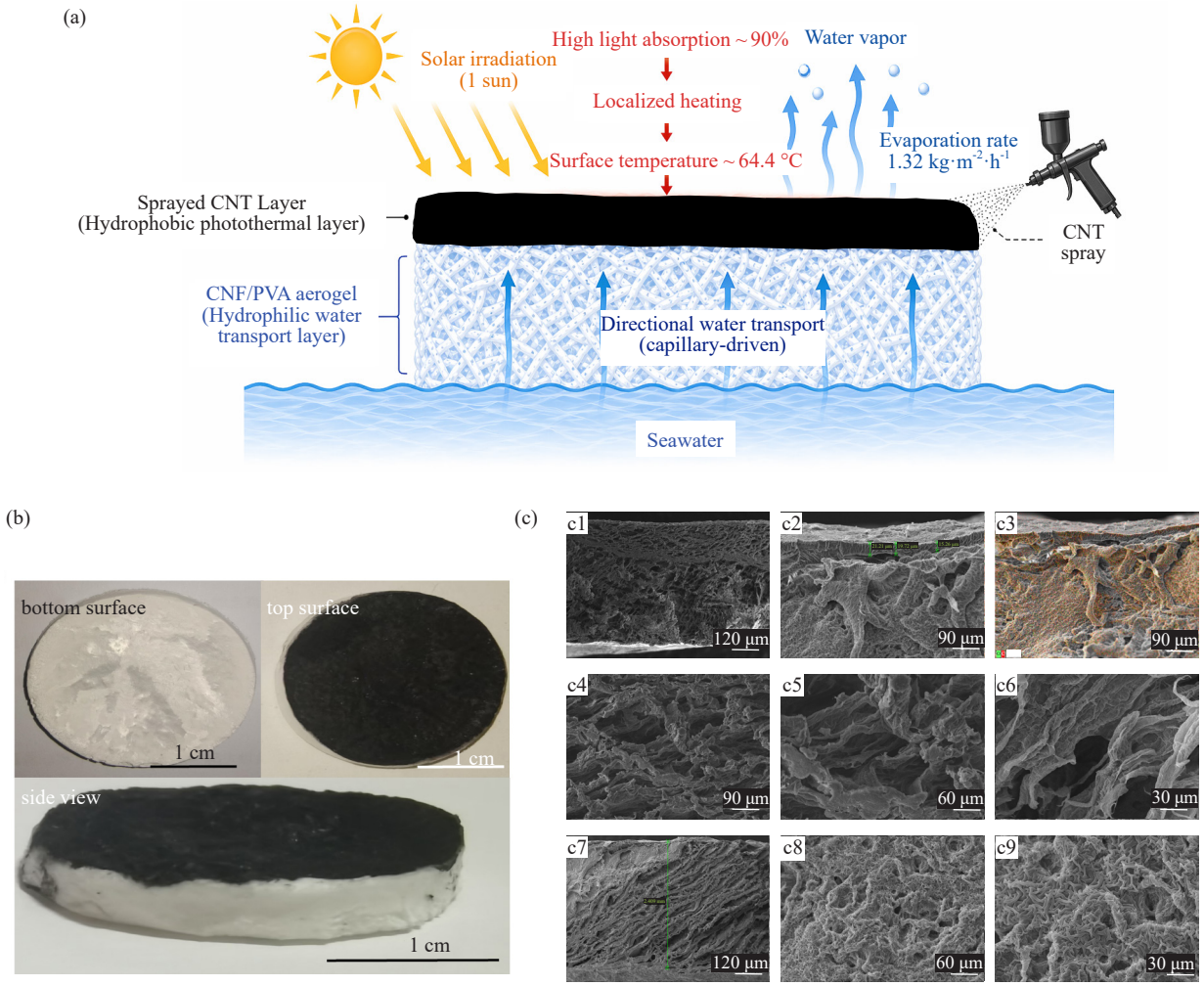

Figure 2. (a) Schematic diagram of the evaporation mechanism of the Janus aerogel; (b) Photographs of the Janus aerogel; (c) SEM images of 6% CPC: (c1-c3) cross-sectional views of the bilayer aerogel with corresponding elemental maps (O marked in green and C marked in red); (c4-c6) the upper photothermal layer; (c7-c9) the PVA/CNF aerogel

As shown in Figure 2b, the aerogel clearly reveals a distinct two-layer asymmetric structure with a clear black-white contrast. As presented in Figure 2c, SEM characterization shows that the 6% CPC sample possesses an abundant

porous structure, which increases the specific surface area, and the photothermal layer has a thickness of approximately 18.73 μm. Although the PVA/CNF aerogel also exhibits a porous structure, its microstructure is significantly different. Specifically, the PVA/CNF aerogel displays an anisotropic porous structure characterized by a dense surface layer and an internal layered, directionally aligned arrangement. The pore size of the surface layer is approximately 5-15 μm, while the internal interlayer channels exhibit pore sizes of about 30-60 μm, indicating significant differences in both microstructure and pore size gradient.

3.2 *Structure and thermal storage properties*

As shown in Figure 3a, in the infrared spectra of aerogels with different CNT loadings, the characteristic absorption peaks of various functional groups are clearly distinguishable. The absorption peak near 3,435 cm^{-1} corresponds to the -OH stretching vibration. The CNT content does not significantly shift the peak position, but the absorption intensity varies slightly, indicating minor changes in the microenvironment of the hydroxyl groups. The peak at 1,634 cm^{-1} corresponds to the C=O stretching vibration, and its position remains largely stable. The absorption intensities at 1,594 cm^{-1} and 1,349 cm^{-1} exhibit notable differences with varying CNT content, suggesting that the photothermal component content can modulate the molecular vibration environment and infrared absorption characteristics of the aerogel. Overall, the introduction of CNT does not cause obvious shifts in the characteristic peaks of the main functional groups but significantly affects the absorption intensities, reflecting a certain degree of alteration in the intermolecular interactions and microscopic electronic structure of the aerogel.

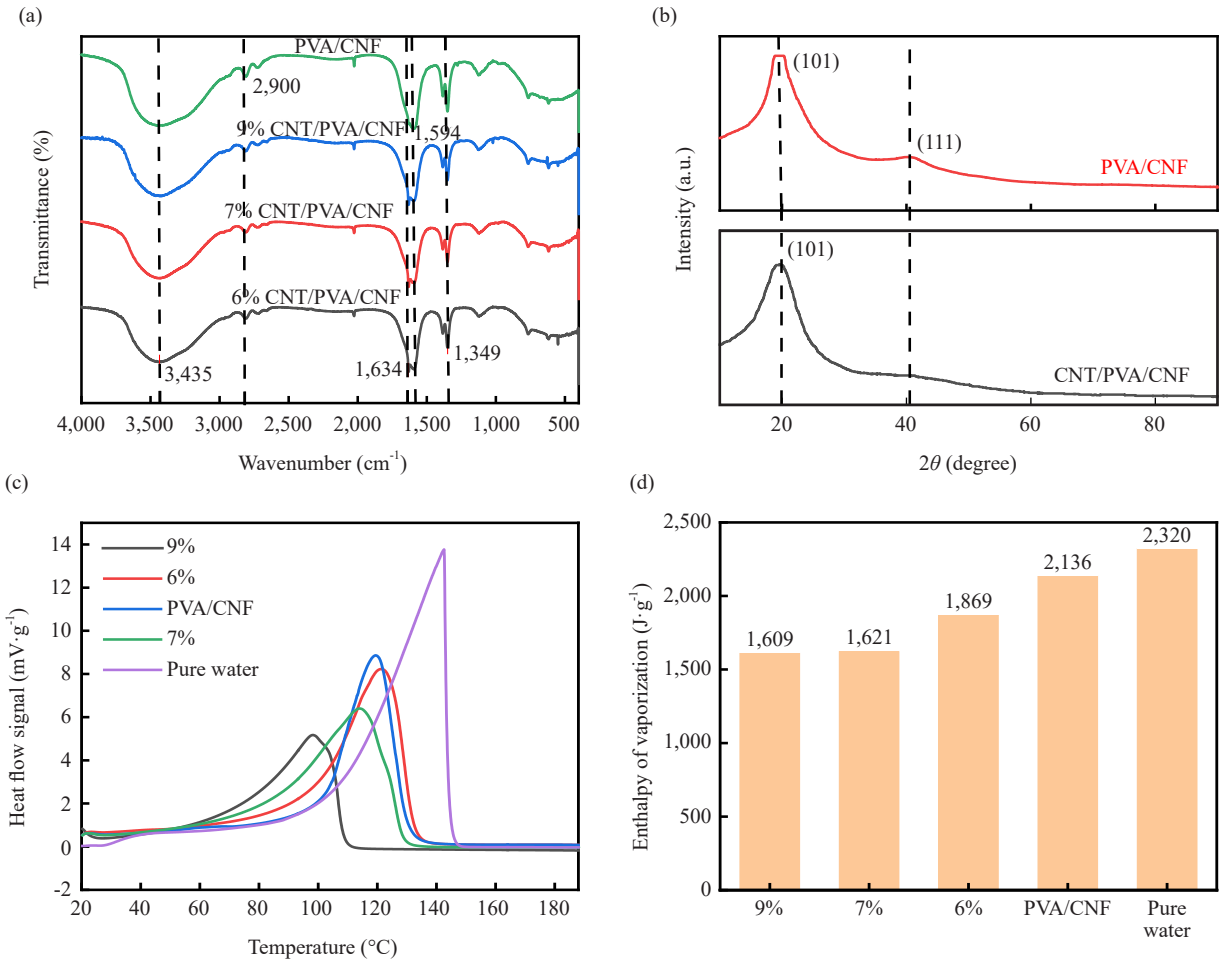

Figure 3. (a) FTIR spectra of 6% CPC, 7% CPC, 9% CPC, and PVA/CNF aerogel; (b) XRD patterns of 9% CPC and PVA/CNF aerogel; (c) DSC curves and (d) equivalent evaporation enthalpy of pure water, PVA/CNF, 6% CPC, 7% CPC, and 9% CPC

As shown in Figure 3b, both the Janus aerogel containing 9% CPC and the pure PVA/CNF aerogel display characteristic diffraction peaks of the (101) and (111) crystal planes at approximately $2\theta = 20°$ and 40°, indicating that the two samples possess similar crystal plane structures. However, distinct differences in the peak positions and shapes are observed, indicating that the introduction of the photothermal component modifies the crystal structure of the aerogel. The pure PVA/CNF aerogel exhibits a high-intensity, sharp main peak, indicating good crystalline order. In contrast, the 9% CPC sample shows significantly reduced and broadened diffraction peaks, suggesting that the addition of CNT disrupts the original crystalline regularity of the aerogel, leading to decreased crystallinity and changes in grain size or perfection. In summary, the introduction of CNT inhibits crystal growth and ordered arrangement by affecting intermolecular interactions, thereby significantly modulating the crystal structural characteristics of the aerogel.

As shown in Figure 3c, the Differential Scanning Calorimetry (DSC) curve of pure water exhibits a narrow and sharp heat flow peak, with the heat flow signal rapidly decaying after the peak, indicating rapid completion of the evaporation process. In contrast, the curves of the PVA/CNF aerogel and aerogel samples with 9%, 7%, and 6% CPC show broad peaks and weaker heat flow signals, reflecting significant differences in the evaporation enthalpy of water within the aerogel compared to pure water. As shown in Figure 3d, the evaporation enthalpy of pure water is 2,320 $J \cdot g^{-1}$, which is generally consistent with the theoretical value of 2,410 $J \cdot g^{-1}$. The evaporation enthalpy of the PVA/CNF aerogel is 2,136 $J \cdot g^{-1}$. For the Janus aerogels with different CNT contents, the evaporation enthalpies are 1,609 $J \cdot g^{-1}$ (9% CPC), 1,621 $J \cdot g^{-1}$ (7% CPC), and 1,869 $J \cdot g^{-1}$ (6% CPC), all lower than that of pure water. This is attributed to the interaction between functional groups in the aerogel and water molecules, which reduces the energy required for water evaporation. Moreover, a higher CNT content leads to lower evaporation enthalpy and thus higher water evaporation rate and efficiency.

3.3 *Wettability and photothermal performance*

As shown in Figure 4a, the pure PVA/CNF aerogel exhibits an initial contact angle of 33°, which decreases to 0° within 0.3 s, demonstrating strong hydrophilicity and rapid water spreading on its surface. All CNT-containing aerogels show initial hydrophobicity: the 6% CPC has an initial contact angle of 115°, dropping to 40° at 1 s and 22° at 2 s; the 7% CPC has an initial contact angle of 116°, decreasing to 28° at 1.2 s and 18° at 1.6 s; and the 9% CPC has an initial contact angle of 118°, decreasing to 39° at 1.5 s and 20° at 2 s. The contact angles of all CNT-containing aerogels decrease significantly over time, indicating gradually enhanced surface wettability, with higher CNT content leading to stronger initial hydrophobicity.

As shown in Figure 4b, in the ultraviolet region of 200-400 nm, the pure aerogel exhibits an absorptance close to 0, while CNT modification greatly improves the absorptance. In the 400-1,400 nm region, the absorptance of the pure aerogel fluctuates and remains generally low, whereas after CNT modification, the absorptance stabilizes at a high level. This is attributed to the unique electronic structure of CNTs, which can interact with Ultraviolet (UV) photons and broaden the UV light absorption range of the aerogel. Higher CNT content results in stronger light absorption capability of the aerogel: the light absorptance values of the 6%, 7%, and 9% CPC are 77%, 97%, and 99%, respectively.

As shown in Figure 4c, during the illumination stage (0-10 min), the temperature of Janus aerogels with different CNT contents increases with time. The 9% CPC shows the fastest heating rate and the highest final temperature (64.4 °C), followed by the 7% CPC (62.8 °C), while the 6% CPC exhibits the slowest heating rate and the lowest final temperature (62.3 °C), indicating that higher CNT content leads to higher photothermal conversion efficiency of the aerogel. During the cooling stage (10-15 min), the temperatures of all three samples decrease rapidly. The 9% CPC shows a faster cooling rate, while the 6% and 7% CPC exhibit similar cooling rates, suggesting that CNT content affects the heat retention capability of the aerogel; the sample with higher CNT content loses heat more rapidly under dark conditions.

As shown in Figure 4d, the 9% CPC composite exhibits only a minor weight loss below 150 °C, attributed to the evaporation of physically adsorbed water, without evident thermal decomposition. This characteristic allows the material to retain its structural and chemical stability under typical operating temperatures of actual evaporation processes (e.g., below 100 °C), thereby demonstrating considerable potential for practical evaporation applications. Moreover, the residual mass of the PVA/CNF sample at 600 °C is 16.4%, which is higher than that of 9% CPC (7.6%). This phenomenon may be attributed to the non-uniform dispersion of carbon nanotubes or weakened interfacial interactions among CNTs, PVA, and CNF, which could facilitate heat transfer and consequently accelerate thermal degradation.

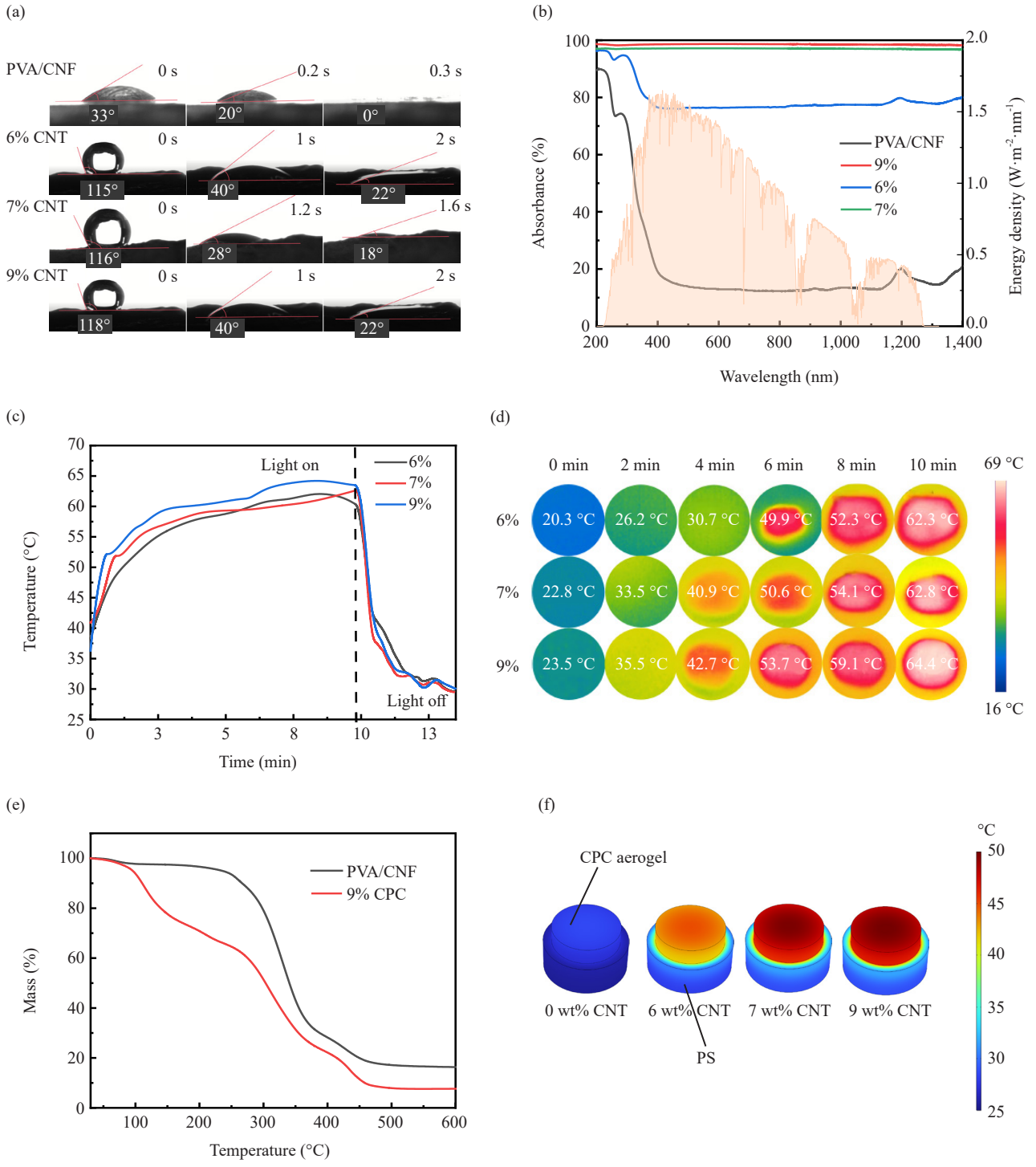

Figure 4. (a) Water contact angle images and (b) absorptance of PVA/CNF, 6% CPC, 7% CPC, and 9% CPC; (c) Photothermal curves and (d) thermal infrared images of 6% CPC, 7% CPC, and 9% CPC; (e) Thermogravimetric (TG) curves of 9% CPC and PVA/CNF composite film; (f) Three-dimensional temperature distribution of aerogels with various CNT loadings following 4 min of illumination from simulation (upper layer: aerogel; lower layer: PS foam)

As shown in the thermal infrared images in Figure 4e, within 0-10 min, the surface temperatures of Janus aerogels with different CNT contents increase with illumination time, and at the same time point, a higher CNT content corresponds to a higher aerogel temperature. As time progresses and CNT content increases, the area of the high-

temperature region gradually expands, indicating continuous heat accumulation and broadening heat distribution within the aerogel. In summary, a higher CNT content results in a more pronounced temperature increase of the aerogel, along with greater heat accumulation and wider heat distribution. Referring to the multi-physics simulation strategy previously reported for Ti_2O_3-based phase-change aerogels [20], finite element-based multiphysics simulations were performed to further investigate the temperature distribution behavior. Simulations were conducted on aerogels with different CNT loadings after 4 min of light irradiation, with Polystyrene (PS) foam used as the thermal insulation substrate (Figure 4f). With increasing CNT doping ratio, the heat accumulation effect at the aerogel surface becomes markedly stronger, reflecting a notable enhancement in the material's photothermal conversion capability. The underlying PS foam retains a low temperature over an extended period, exhibiting superior thermal insulation performance and considerably minimizing conductive heat loss to the bulk water. To validate the finite element simulation, we compared the simulated surface temperature with experimental infrared thermography measurements (Figure 4e). For the 9% CPC aerogel after 4 min of illumination, the simulation yields a maximum surface temperature of approximately 45.6 °C, whereas the experimentally measured temperature under identical conditions is 42.7 °C. This slight overestimation (about 2.9 °C) can be attributed to several factors. First, the simulation does not consider evaporative cooling at the air-water interface, which lowers the actual surface temperature. Second, the simulation assumes a uniform ambient temperature of 25 °C, while in the experiment, the air surrounding the evaporator may be slightly warmed by radiative and convective heat transfer, effectively reducing the temperature gradient. Despite these minor discrepancies, the simulation correctly reproduces the experimental trend of increasing surface temperature with higher CNT loading, thereby confirming the qualitative reliability of the model for predicting the photothermal behavior of the Janus aerogel.

3.4 *Evaporation performance test*

As shown in Figure 5a, b, under 1 sun, a higher CNT content leads to a faster mass loss rate of water evaporation. When the CNT content increases from 6% to 9%, the evaporation rate and efficiency exhibit an overall upward trend. Specifically, the evaporation rates of the 6%, 7%, and 9% CPC are 1.08, 1.19, and 1.32 $kg \cdot m^{-2} \cdot h^{-1}$, respectively, and the corresponding evaporation efficiencies are 72.30%, 79.66%, and 88.37%, all significantly higher than those of seawater (0.43 $kg \cdot m^{-2} \cdot h^{-1}$, 28.79%) and the control group, PVA/CNF (0.66 $kg \cdot m^{-2} \cdot h^{-1}$, 44.18%), confirming that CNT effectively enhances the evaporation performance of the aerogel. Table 2 summarizes the key properties of Janus aerogels as a function of CNT loading.

Table 2. Summary of the performance of Janus aerogels as a function of CNT loading (6% CPC, 7% CPC, and 9% CPC)

Property/performance	6% CPC	7% CPC	9% CPC
CNT loading (wt%)	6	7	9
Initial water contact angle (°)	115	116	118
Light absorptance (%)	77	97	99
Evaporation rate ($kg \cdot m^{-2} \cdot h^{-1}$)	1.08	1.19	1.32
Evaporation efficiency (%)	72.30	79.66	88.37

As shown in Figure 5c, d, when the light intensity increases from 1 sun to 2 sun, the evaporation rate of the 9% CPC rises from 1.32 $kg \cdot m^{-2} \cdot h^{-1}$ to 2.51 $kg \cdot m^{-2} \cdot h^{-1}$. Moreover, a higher light intensity results in a more significant mass reduction within the same time period. The 6% CPC exhibits a certain evaporation capability, but there is still room for improvement. As the CNT content increases to 7% and 9%, the evaporation rate and efficiency are significantly enhanced. At the microscopic level, a higher CNT content enlarges the light absorption area and increases the number of energy conversion sites. These sites efficiently convert absorbed light energy into thermal energy, intensifying the thermal motion of water molecules within the aerogel, making it easier for them to escape as vapor by overcoming

surface binding forces, thereby accelerating the evaporation process.

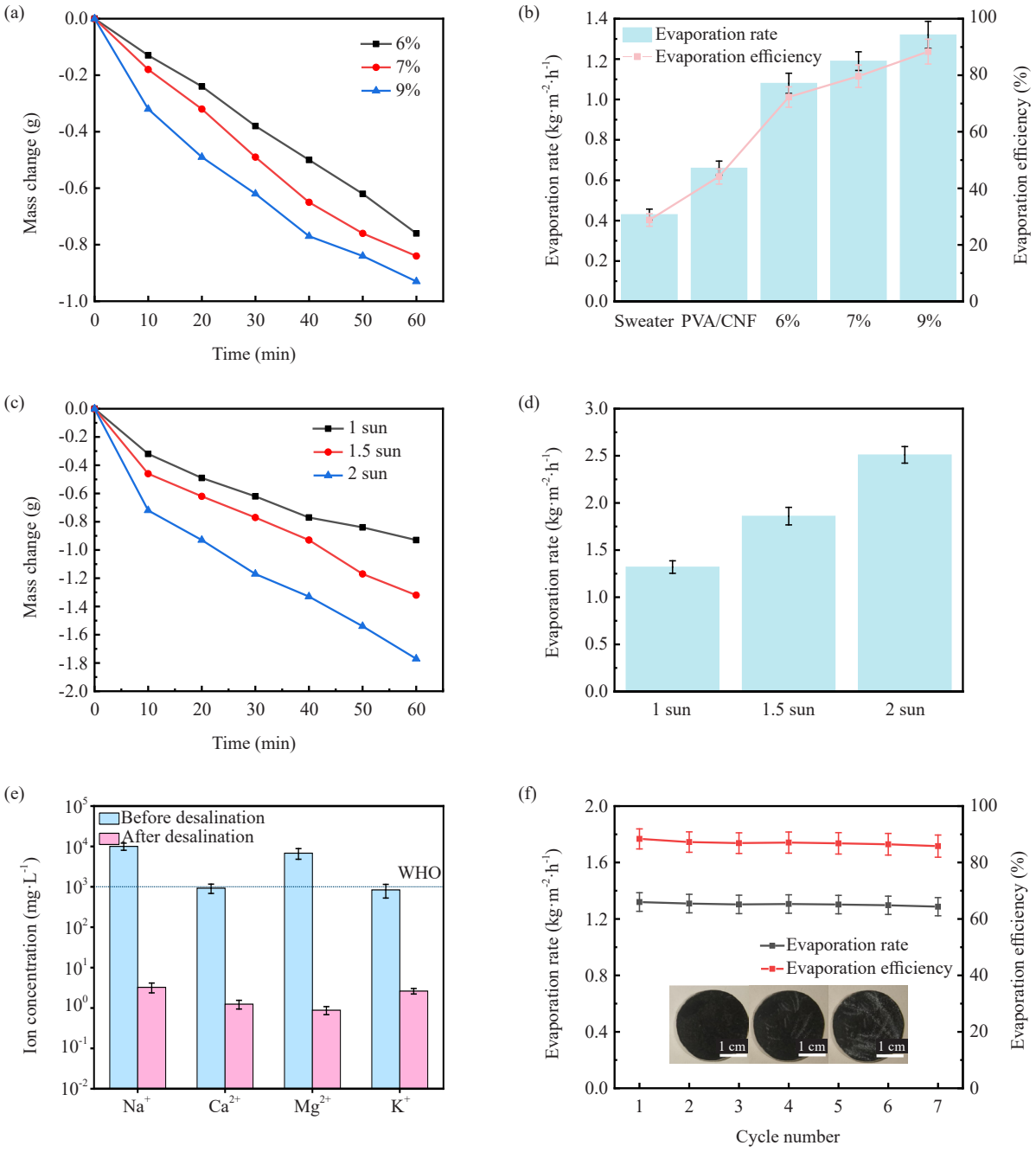

Figure 5. (a, b) Evaporation amount, rate, and efficiency of 6% CPC, 7% CPC, and 9% CPC under 1 sun; (c, d) Evaporation amount, rate, and efficiency of 9% CPC under different solar light intensities; (e) Comparison of Na^+, Ca^{2+}, Mg^{2+}, and K^+ concentrations in collected water with WHO drinking water limits; (f) Evaporation rate and efficiency of 9% CPC Janus aerogel during cyclic operation (inset: surface salt precipitation after 2 h under 1 sun)

To evaluate the quality of the produced water, the concentrations of the major cations (Na^+, K^+, Ca^{2+}, and Mg^{2+}) in the collected condensate were measured. As shown in Figure 5e, the concentrations of all tested ions decreased significantly after the solar evaporation process. Importantly, the concentration of each ion in the condensate is well below the World Health Organization (WHO) drinking water standards, indicating that the water produced by our Janus

aerogel evaporator meets the requirements for drinking water. The quality of the produced water is comparable to that reported in recent studies on solar evaporators [21].

As shown in the inset of Figure 5f, under 1 sun, only a small amount of salt residue is observed on the surface of the 9% CPC Janus aerogel after 2 h of irradiation, and no continuous salt crystallization layer is formed. This indicates that the Janus structure effectively retards salt accumulation during the tested period.

Figure 5f shows that during repeated cycling of the sample, the evaporation rate and efficiency exhibit an overall decreasing trend. The initial evaporation rate is approximately 1.32 $kg \cdot m^{-2} \cdot h^{-1}$, which decreases to about 1.29 $kg \cdot m^{-2} \cdot h^{-1}$ after the seventh cycle. The initial evaporation efficiency is about 88.37%, which drops to about 85.70% after the seventh cycle. Although the cycling performance of this aerogel shows slight degradation, the overall evaporation performance remains relatively stable.

To place our evaporation performance in the context of the literature, we compared the Janus aerogel developed in this study with several representative CNT-based solar evaporators. Many reported systems employ substantially higher CNT loadings to achieve competitive evaporation rates. For instance, Si et al. fabricated a three-dimensional PAN/CNTs foam with a CNT content of 17 wt% and obtained a pure-water evaporation rate of 2.04 $kg \cdot m^{-2} \cdot h^{-1}$ under 1 sun [22]. Another study reported a Janus Bacterial Cellulose/Sodium alginate (J-BCS)/CNT 40% aerogel containing 40 wt% CNT, which reached an evaporation rate of 1.95 $kg \cdot m^{-2} \cdot h^{-1}$ in pure water [23]. In contrast, our 9% CPC Janus aerogel achieves an evaporation rate of 1.32 $kg \cdot m^{-2} \cdot h^{-1}$ and an efficiency of 88.37% in simulated seawater using only 9 wt% CNT. Even when compared with a high-performance MWCNTs-SPNG Janus evaporator (evaporation rate of 2.49 $kg \cdot m^{-2} \cdot h^{-1}$ and efficiency of 91% [11]), our material attains a comparable efficiency (88.37% vs. 91%), albeit with a modest sacrifice in evaporation rate. Considering the cost and sustainability of the photothermal material, this work demonstrates a favorable balance between CNT consumption and evaporation performance.

3.5 *Heat loss analysis*

The heat losses via conduction, radiation, and convection were evaluated for the 6% CPC, 7% CPC, and 9% CPC samples after reaching steady-state temperature under 1 sun illumination. The calculated values are summarized in Table 3.

As shown in Table 3, the 6% CPC sample exhibits the lowest conductive heat flux (0.108 W), thermal radiation flux (0.099 W), and convective heat flux (0.071 W), corresponding to loss fractions of 10.8%, 12.3%, and 8.8%, respectively. With increasing CNT content, all three loss components increase slightly due to the higher surface temperature. For the 9% CPC sample, the conductive, radiative, and convective losses are 0.162 W (16.2%), 0.128 W (15.9%), and 0.089 W (11.1%), respectively.

Notably, conductive heat loss to the bulk water is effectively suppressed by the PS foam insulation layer, resulting in lower conductive loss compared to radiative and convective losses for all samples. This confirms the excellent heat localization capability of our Janus aerogel evaporator.

Table 3. Per-sample thermal loss characteristics

Sample	ΔT/°C	T/K	T_{amb}/K	Q_{cond}/W	η_1	Q_{rad}/W	η_2	H_{conv}/W	η_3
6% CPC	0.2	323.25	303.15	0.108	10.8%	0.099	12.3%	0.071	8.8%
7% CPC	0.2	324.85	303.15	0.108	10.8%	0.108	13.4%	0.077	9.6%
9% CPC	0.3	328.45	303.15	0.162	16.2%	0.128	15.9%	0.089	11.1%

4. Conclusion

A Janus-type aerogel was successfully fabricated by preparing a PVA/CNF aerogel substrate via freeze-drying and subsequently loading a CNT photothermal layer through a spray-coating process. The resulting aerogel

exhibits a uniform pore size distribution and a well-defined functional interface. The PVA/CNF aerogel shows strong hydrophilicity, while the initial contact angle of the Janus aerogel increases with higher CNT content. Under 1 sun, the 9% CPC Janus aerogel demonstrates the fastest heating rate, reaching a maximum surface temperature of 64.4 °C, an evaporation rate of 1.32 $kg \cdot m^{-2} \cdot h^{-1}$, and an evaporation efficiency of 88.37%. When the light intensity was increased to 2 sun, the evaporation rate rose to 2.51 $kg \cdot m^{-2} \cdot h^{-1}$, indicating a clear linear response of the system to solar energy input. After seven cycles of operation in simulated seawater, the evaporation rate decreased by only 5%, and only minor salt residue was observed on the surface after 2 hours, which is attributed to the salt-inhibiting effect of the hydrophobic photothermal layer and the stable water transport capability of the hydrophilic substrate within the Janus structure. Owing to its excellent photothermal evaporation performance and good cyclic stability over 7 cycles, this Janus aerogel holds great practical application potential in seawater desalination and distributed solar-powered water purification devices.

CRediT authorship contribution statement

Liumin Luo: Writing—original draft, Visualization, Data curation, Conceptualization. Airong Wang: Writing—review & editing, Visualization, Validation. Luhan Zheng: Conceptualization, Methodology, Investigation. Xiaxuan Jia: Validation. Ge Shi: Validation. Yizhen Li: Supervision, Writing—review. Jin Peng: Supervision, Funding acquisition. Mengya Shang: Resources, Validation, Funding acquisition.

Acknowledgments

This paper is based upon work supported by the Henan University of Technology Young Backbone Teacher Training Plan (No. 21421260), the Henan Province Key R & D Special Project (No. 241111233100).

Conflict of interest

The authors declare that they have no known competing financial interests or personal relationships that could have appeared to influence the work reported in this paper.

References

[1] Y. Song, X. Hu, M. Wang, J. Bai, S. Ma, and S. Tong, "Calla lily-inspired 3D evaporator: a dual interface design for enhanced solar water evaporation," *Desalination*, vol. 597, pp. 118361, 2025.

[2] M. Irshad, G. Maqsood, N. Arshad, B. Shakoor, I. Ahmed, M. Ali, M. Asghar, W. Li, W. Li, N. Mushtaq, et al., "Interfacial engineering and hydrophilic/hydrophobic coatings in solar evaporators: strategies for balancing evaporation and condensation-a comprehensive review," *Small*, vol. 22, no. 10, pp. e06124, 2026.

[3] W. Liao, C. Du, L. Li, D. Wang, Y. Wu, J. Luo, J. Deng, Y. Huang, P. Wang, and Y. Yang, "Electrospun PANI/CB-PEN nanofiber composite membranes for efficient solar interfacial evaporation," *Journal of Applied Polymer Science*, vol. 142, no. 30, pp. e57224, 2025.

[4] J. Zong, D. Wang, H. Yang, B. Lu, D. Huang, X. Wang, S. Li, and X. Zang, "Hydrophilic photothermal polydopamine/polyurethane foam for efficient solar-driven water evaporation," *Journal of Applied Polymer Science*, vol. 142, no. 18, pp. e56832, 2025.

[5] C. Tang, J. Hu, T. Yue, X. Hu, W. Yu, and H. Lei, "Harnessing photothermal graphene oxide interlayers for high-flux solar-driven pervaporation desalination," *Separation and Purification Technology*, vol. 392, pp. 137136, 2026.

[6] W. Wu, X. Han, and X. Gong, "Stable superhydrophobic interfacial solar evaporator based on CuS@CdS hybrid photothermal composites towards ultrahigh-efficiency seawater evaporation," *Applied Energy*, vol. 375, pp. 124099, 2024.

[7] B. Yu, Y. Wang, Y. Zhang, and Z. Zhang, "Nanoporous black silver film with high porosity for efficient solar steam generation," *Nano Research*, vol. 16, no. 4, pp. 5610-5618, 2023.
[8] Z. Wang, Y. Zhang, M. Chen, L. Wang, J. Shen, P. Senin, T. Bian, and X. Zhu, "Solar-driven 3D photothermal-adsorptive composite evaporator enables simultaneous seawater desalination and ultra-selective lithium extraction," *Chemical Engineering Journal*, vol. 532, pp. 174609, 2026.
[9] C. Yang, F. Zhao, R. Jia, W. Agbley, Y. Liu, H. Ma, X. Wang, and J. Xing, "Heating jacket-like janus CS/PPy aerogel with gradient-oxidation for high-efficiency solar desalination," *Chemical Engineering Journal*, vol. 530, pp. 173390, 2026.
[10] Y. Zhang, H. Wang, and J. Zhang, "Application of graphene-based solar driven interfacial evaporation-coupled photocatalysis in water treatment," *Catalysts*, vol. 15, no. 4, pp. 336, 2025.
[11] H. Ge, Z. Fang, S. Wu, J. Qiu, X. Liu, and Z. Zhang, "Efficient solar-driven interfacial evaporation and desalination using simple, salt-resistant, carbon nanotube-based janus evaporators," *Energy*, vol. 306, pp. 132354, 2024.
[12] Z. Wang, W. Tu, Y. Zhao, H. Wang, H. Huang, Y. Liu, M. Shao, B. Yao, and Z. Kang, "Robust carbon-dot-based evaporator with an enlarged evaporation area for efficient solar steam generation," *Journal of Materials Chemistry A*, vol. 8, no. 29, pp. 14566-14573, 2020.
[13] D. Wang, X. Lin, Y. Wu, L. Li, W. Feng, Y. Huang, and Y. Yang, "Hanging photothermal fabric based on polyaniline/carbon nanotubes for efficient solar water evaporation," *ACS Omega*, vol. 8, no. 47, pp. 44659-44666, 2023.
[14] S. Liu, S. Wang, S. Shuai, Y. Weng, and F. Zheng, "Efficient solar desalination of seawater using a novel carbon nanotube-based composite aerogel," *Materials*, vol. 16, no. 17, pp. 5815, 2023.
[15] D. Ji, B. Zhang, F. Jia, A. Wei, Y. Yuan, and H. Zhao, "Carbon nanotube-enhanced photothermal conversion thermosensitive hydrogel for solar water evaporation: preparation and performance," *Reactive and Functional Polymers*, vol. 217, pp. 106462, 2025.
[16] J. Su, A. Xing, J. Hu, Y. Wu, J. Zhou, J. Xu, and X. Wang, "Janus-structured wood-based evaporator: electrospun lignin carbon nanofibers (LCNFs) with in situ Fe_3O_4 growth enable solar-driven seawater desalination and purification," *Desalination*, vol. 625, pp. 119937, 2026.
[17] G. Chen, H. Zhang, Z. Chen, M. Chen, T. Liu, J. He, L. Jiang, Y. Chen, and J. Wang, "MoS_2-decorated solar evaporation aerogel with sugarcane vertically aligned channels for water desalination and purification," *ACS Sustainable Chemistry & Engineering*, vol. 14, no. 9, pp. 4569-4582, 2026.
[18] P. Wang, W. Zhang, Q. Yuan, T. Mai, M. Qi, and M. Ma, "3D Janus structure MXene/cellulose nanofibers/luffa aerogels with superb mechanical strength and high-efficiency desalination for solar-driven interfacial evaporation," *Journal of Colloid and Interface Science*, vol. 645, pp. 306-318, 2023.
[19] Z. Chang, Y. Pan, Y. Zhang, and X. Wu, "High-porosity hydrophobic (expand PVA)/(expand CNF) aerogels loaded with tetradecane for phase change cold storage," *Chemical Engineering Journal*, vol. 526, pp. 171449, 2025.
[20] L. Zheng, M. Shang, A. Wang, X. Jia, H. Gao, J. Li, J. Yu, and J. Peng, "Ti_2O_3-based phase-change aerogels with synergetic photothermal-latent heat storage for all-day desalination," *Applied Thermal Engineering*, vol. 298, no. 3, pp. 131140, 2026.
[21] Y. Liu, R. Feng, Y. Zhao, X. Guo, J. Ding, S. Liu, Y. Wang, J. Zhu, and X. Li, "Solar-mechano symbiosis dual-mode janus bioaerogel for context-adaptive atmospheric water harvesting beyond solar reliance," *Advanced Materials*, vol. 37, no. 45, pp. e12244, 2025.
[22] J. Si, K. Lan, Z. Cui, Q. Wang, S. Zeng, X. Liu, and C. Gong, "Constructing salt-resistant 3D foams with hierarchical interconnected channels by vacuum casting method for efficient solar evaporation of hypersaline water," *Desalination*, vol. 576, pp. 117339, 2024.
[23] F. Wang, S. Zhao, G. Wei, and Z. Su, "Bacterial cellulose-based janus energy storage phase change composite aerogel for efficient interfacial solar vapor generation," *Separation and Purification Technology*, vol. 356, no. B, pp. 129983, 2025.